

Article

Quantitative Morphology of Epithelial Folds

Nick Štorgel,^{1,2} Matej Krajnc,^{1,*} Polona Mrak,³ Jasna Štrus,³ and Primož Ziherl^{1,2,4}¹Jozef Stefan Institute, Ljubljana, Slovenia; ²Faculty of Mathematics and Physics and ³Biotechnical Faculty, University of Ljubljana, Ljubljana, Slovenia; and ⁴Erwin Schrödinger International Institute for Mathematical Physics, University of Vienna, Vienna, Austria

ABSTRACT The shape of spatially modulated epithelial morphologies such as villi and crypts is usually associated with the epithelium-stroma area mismatch leading to buckling. We propose an alternative mechanical model based on intraepithelial stresses generated by differential tensions of apical, lateral, and basal sides of cells as well as on the elasticity of the basement membrane. We use it to theoretically study longitudinal folds in simple epithelia and we identify four types of corrugated morphologies: compact, invaginated, evaginated, and wavy. The obtained tissue contours and thickness profiles are compared to epithelial folds observed in invertebrates and vertebrates, and for most samples, the agreement is within the estimated experimental error. Our model establishes the groove-crest modulation of tissue thickness as a morphometric parameter that can, together with the curvature profile, be used to estimate the relative differential apicobasal tension in the epithelium.

INTRODUCTION

Many epithelial morphologies are spatially modulated rather than flat, the best-known examples being villi and crypts in the mammalian small intestine. These formations serve a specific physiological function closely related to their shape—the protruding villi increase the area for absorption of nutrients, and the recessed crypts contain glands secreting mucus and enzymes—so their shape must be robust. This applies even more to embryonic epithelia responsible for the initial development of the body plan, including key transformations such as gastrulation or neurulation.

The robustness of shape is best ensured by relying on simple biophysical processes. From the mechanical perspective, villi, crypts, and various types of epithelial folds are most straightforwardly seen as a buckling instability of a layer attached to a substrate of smaller area (1,2). Area mismatch can lead to wrinkles, creases, and ridges, as well as simple and period-doubled folds (3,4). Also possible are more complex shapes such as zig-zag and labyrinthine folds and various villus- and crypt-like morphologies (5–11). Area mismatch is usually related to the differential growth of the epithelium and the supporting tissue, which may depend on the local shape of the epithelium so as to promote either evaginated or invaginated folds (5), thereby distinguishing between villi and crypts.

The buckling theory is nontrivial but intuitive (3,12–15), yet by treating the tissue locally as a homogeneous layer, it disregards the apicobasal polarity present in all simple

epithelia. The apical, lateral, and basal domains of the cell membrane are biochemically and functionally distinct, implying that their mechanical properties must be different, too. In part, the differences can be due to the distribution of cell-adhesion molecules such as cadherins and integrins, which localize at the lateral and basal domains and render the effective surface tension of these domains smaller than that of the apical domain. This is nicely illustrated by the shape of adhering mouse embryonic cells which shows that the cell-lumen interface is less tense than the cell-cell contact zone, suggesting that adhesion decreases membrane tension (16). Another microscopic mechanism contributing to the differential effective tensions is the distinct pattern of myosin organization within the cell. For example, in *Drosophila* ovary follicle epithelium, apical myosin forms a random polygonal mesh, whereas basal myosin is arranged in parallel fibers with a more even, albeit polarized, in-plane distribution (17), so that one can distinguish between the apical constriction and the basal contraction modes. The mechanical aspects of cell apicobasal polarity can also be witnessed in the curling of *Xenopus* embryonic epithelium peeled off the inner ectoderm, as well as by the folding of explants into spherules (18) or by the formation of epithelial vesicles in *std* mutant *Drosophila* embryos (19). These spontaneous deformations are consistent with the presence of intraepithelium stresses favoring curved over flat tissue shape. Generated by actomyosin contractility, cell-cell adhesion, and other related cell-level mechanisms (16,20–22), these stresses could also be responsible for the complex epithelial morphologies.

This hypothesis is not at odds with the buckling theory, because both mechanisms may well act simultaneously, but its conceptual framework is different in several ways. First, it interprets the epithelial morphology in terms of

Submitted August 10, 2015, and accepted for publication November 12, 2015.

*Correspondence: matej.krajnc@ijs.si

Nick Štorgel and Matej Krajnc contributed equally to this work.

Editor: Stanislav Shvartsman.

© 2016 by the Biophysical Society

0006-3495/16/01/0269/9



<http://dx.doi.org/10.1016/j.bpj.2015.11.024>

the intrinsic preferred shape of cells and does not rely exclusively on the antagonism between the tissue and the substrate. Second, the substrate (which is still needed to ensure that the epithelium is globally planar across a large enough distance) may be liquid-like and thus free of the permanent shear stresses characteristic of the buckling theories. This is more consistent with the view that on long time-scales, supporting tissues can be remodeled in response to stress. Finally, intraepithelium forces alone combined with confinement typical for embryos of most animal species can reproduce certain morphogenetic transformations at a stage when the elastic support is absent or not well developed, e.g., during gastrulation and neurulation (23–25).

So far, the intraepithelium stress hypothesis has been explored within two related physical models. In one of them, cell shape is determined by effective surface tensions of the basal, lateral, and apical sides and cytoplasm is treated as an incompressible fluid (26). This model was used to interpret the formation of the ventral furrow in *Drosophila* as a collective process involving all of the embryo (27) and to demonstrate that the intraepithelium stresses alone can reproduce the well-developed longitudinal folds seen, e.g., in the stomach of an ascidian tunicate *Styela clava* (28). A somewhat different approach where the apical surface tension is replaced by the circumferential line tension of the actin cable was employed to interpret the bending and buckling of flat tissues, as well as the stability of epithelial spherules and tubes (29).

The theoretical fold morphologies obtained within the basic surface tension model (28) are encouraging as a proof-of-principle support of the intraepithelium stress hypothesis, but they fall short of reproducing in detail the broad spectrum of experimental observations. This suggests that although the apicobasal tension may drive folding, it is not the only force that shapes the tissues. Here, we generalize the basic model by including the basement membrane, a thin extracellular matrix composed of collagen fibers and laminins separating the epithelium from the connective tissue. Our improved theory is anatomically more faithful and provides a more definite test of the hypothesis, because it shows that the folds are stable despite the bending rigidity of the membrane. Although it partly counterbalances the intraepithelial stresses, the membrane leads to a greater variety of folds, which can be divided into four distinct types identified in various invertebrate and vertebrate epithelia. Most fold types are characterized by a pronounced groove-to-crest tissue thickness modulation, and by screening the folds using the proposed classification and measuring the modulation, one can infer the relative apical and basal tensions of cells.

MATERIALS AND METHODS

Histological micrographs in Fig. 3, A**, D*, D**, and E*, were taken from the collection of histological sections at the Department of Biology, Biotechnical Faculty, University of Ljubljana. Sections were inspected

and imaged by light microscope Zeiss (Oberkochen, Germany) AxioImager Z.1 equipped with a HRc AxioCam camera and Axiovision software.

Surface-tension model

Our model relies on the differential adhesion hypothesis (30), treating cells in a medium as incompressible droplets characterized by cell-cell and cell-medium surface tensions, the shape of the cell aggregate minimizing the total surface energy. In a monolayer tissue, tensions of cell-lumen, cell-cell, and cell-basement-membrane contacts can be attributed to a cell's cortex tension, σ , to differential tension, η , associated with apicobasal polarity, and to cell-cell adhesion strength, γ (26). Apart from the three surface terms, the tissue energy includes a term representing the elasticity of the basement membrane. Indentation experiments suggest that the membrane does behave as an isotropic solid material with a well-defined Young modulus (31), so that its low-energy deformation mode is bending just like in thin plates; we further assume that during fold formation, cells can glide on the membrane so that any stretching stresses are absent (32). In this case, we can approximate the elastic energy of the membrane by the Kirchhoff-Love theory (33), which for parallel straight folds reduces to $W_{\text{bend}} = (K_{\text{bend}}/2) \int C_{\text{bend}}^2 dA$. Here, K_{bend} and C_{bend} are the bending rigidity and the local curvature of the membrane, respectively, and the integral goes over its area. This continuum model describes the bending elasticity of the membrane; other aspects of its mechanical behavior, such as stress-induced rearrangement of the network of fibers forming the membrane, are more easily included in agent-based models (34,35).

The total energy of the model epithelium and the basement membrane studied here thus reads

$$W = \sigma(A_a + A_b + A_l) + \eta(A_b - A_a) - \frac{\gamma}{2}A_l + W_{\text{bend}}, \quad (1)$$

where A_a , A_b , and A_l are the sums of surface areas of the apical, basal, and lateral cell sides, respectively. As σ , η , and γ cannot be measured directly, we turn to an equivalent representation that involves the effective tensions of the different cell sides—the apical, basal, and lateral tension of $\Gamma_a = \sigma - \eta$, $\Gamma_b = \sigma + \eta$, and $\Gamma_l = 2\sigma - \gamma$, respectively. In all the results presented here, apical tension is the same in all cells, as are basal and lateral tension.

Much as most models of epithelial in-plane structure are reduced to its en face view (36), folds and related morphologies are usually studied by considering the representative tissue cross section (37). We too resort to this simplification to expose the mechanisms at work and to dispose of tissue topology, which is subdominant in this context. The approximation made is controlled in that it replaces the true scaling of cell side area with cell volume by that derived for the cross section, and it does not affect the relative apical and basal surface energies responsible for fold formation.

Here, the tissue cross section (Fig. 1 A) is represented by a chain of quadrilateral cells with straight edges supported by a basement membrane of local curvature C_{bend} (Fig. 1, B and C). By assuming that the dimension of cells along the folds is constant, the fixed-cell-volume constraint is translated into a fixed-area constraint for the quadrilaterals ($A = \text{const.}$). The characteristic length scale is then \sqrt{A} and the energy per unit length along the folds is expressed in units of $\Gamma_l \sqrt{A}$. Using the reduced apical and basal tensions, as well as the reduced bending modulus of the basement membrane, defined by

$$\alpha = \frac{\Gamma_a}{\Gamma_l}, \beta = \frac{\Gamma_b}{\Gamma_l}, \text{ and } \kappa = \frac{K_{\text{bend}}}{\Gamma_l A}, \quad (2)$$

respectively, the dimensionless tissue energy reads

$$w = \alpha l_a + \beta l_b + \frac{1}{2} l_l + \frac{\kappa}{2} \int c_{\text{bend}}^2 ds. \quad (3)$$

Here l_a , l_b , and l_l are sums of the reduced apical, basal, and lateral edge lengths, respectively, measured in units of \sqrt{A} ; $c_{\text{bend}} = C_{\text{bend}}\sqrt{A}$ is the dimensionless curvature of the basement membrane and the integral goes along the membrane contour.

The equilibrium cross sections of the model epithelium are obtained by numerically minimizing the energy (Eq. 3) at given α , β , and κ using periodic boundary conditions to enforce the global planarity of epithelium, varying the wavelength of the fold and the number of cells in it. This is done within the Surface Evolver package (38), and the contour of the basement membrane is discretized such that it coincides with the basal sides of cells. Our code also includes a routine that prevents cell-cell overlap by mimicking hard-core repulsion between nonneighboring cells (Section S1 in the Supporting Material).

RESULTS

Fig. 1 D shows the phase diagram at fixed reduced apical tension $\alpha = 0.6$ in the regime where the reduced basal tension is large enough so that the preferred shape of cells is basally constricted and thus wedge-shaped. Not all cells in the epithelium can assume the preferred shape because of the bending rigidity of the basal membrane and because of the substrate-enforced global planar nature of the tissue. Nonetheless, the total energy of the fold morphology is energetically favorable compared to the flat epithelium provided that the magnitude of the differential tension is neither too small nor too large (28) (Section S1). As a result, intraepithelial stresses do lead to compact, invaginated, evaginated, and wavy fold morphologies, described below and illustrated by characteristic waveforms in points C1, I1, E, and W, respectively, in Fig. 1 D; a more detailed discussion

of fold shapes is presented in Section S2. At fixed reduced basal tension $\beta = 0.6$, we find somewhat different variants of compact and invaginated folds (waveforms C2 and I2 in Fig. 1 E), but evaginated and wavy folds are absent.

Compact folds

This type of epithelium is stable at large enough differential tension and small basement-membrane bending modulus. In this regime, a large fraction of cells in the waveform undergo constriction and are tall; in waveform C1 in Fig. 1 D, the basally constricted cells form the crest and face the lumen. On the other hand, the groove consists of short trapezoidal cells. Contours of the epithelium-lumen interface and of the basement membrane are both notched. Compact folds differ from the other fold morphologies in wavelength and amplitude, which are both comparable to cell size; in waveform C1, they are about twice the average cell height. Note that many cells on the opposite sides of the groove are pushed against each other, showing that this repulsion, too, shapes the waveform. In fact, as basal tension is increased at fixed bending modulus, this effect prevails over the bending rigidity of the basement membrane (Section S1).

At large apical and small basal tension, compact folds consist of tall apically constricted cells forming the groove and less numerous short cells forming the crest (waveform C2 in Fig. 1 E), yet the overall shape of the tightly packed waveform is rather similar to that at large β and small α .

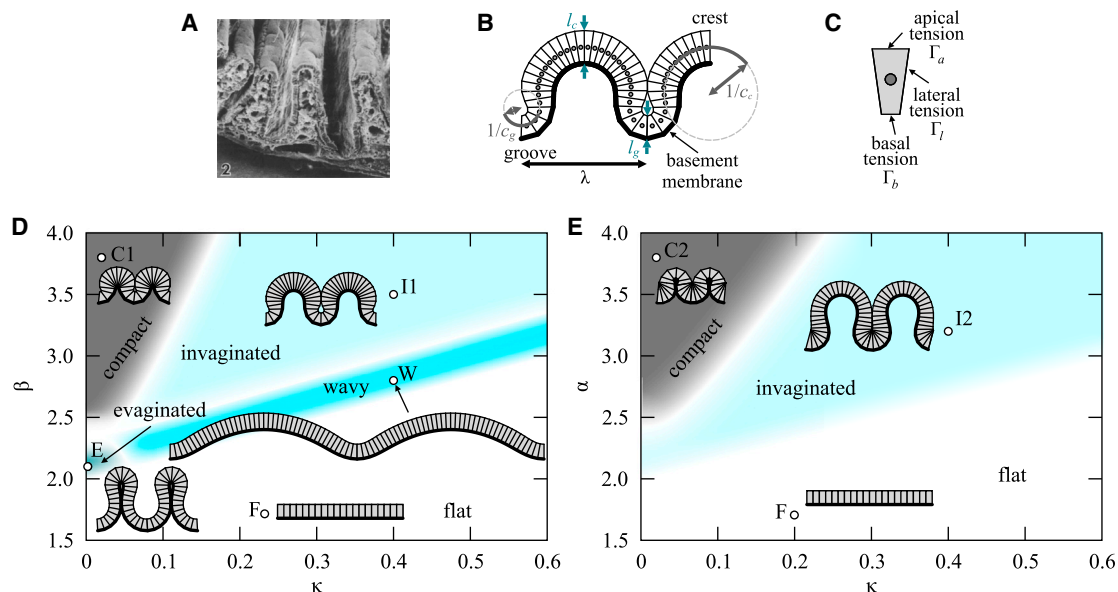


FIGURE 1 Longitudinal folds in the gastric epithelium of *Styela clava* (A; reproduced with permission of Integrative and Comparative Biology from Ermak (44)). (B) The model cross section, showing groove and crest curvatures, c_g and c_c , respectively, and fold wavelength λ ; also plotted is the basement membrane (thick black line). (C) The preferred cell shape is determined by the relative tensions of the apical, lateral, and basal sides. (D and E) Phase diagrams of the fold morphologies for the fixed-apical-tension case in the $(\kappa, \beta > \alpha = 0.6)$ plane (D) and the fixed-basal-tension case in the $(\kappa, \alpha > \beta = 0.6)$ plane (E), showing compact, invaginated, evaginated, and wavy folds. The color shading shows the regions of the phase diagram where the different fold morphologies are stable. The boundaries between these regions are guides to the eye. To see this figure in color, go online.

Finally, the plots are neither perfectly smooth nor perfectly symmetric due to the rather small number of cells in a waveform, typically between 15 and 45 depending on fold type. This artifact of the discrete model used mostly affects the curvature profiles (Fig. 2, *B* and *F*), because the local curvature is calculated from the position of the geometric centers of three neighboring cells. In the segments of waveform with a very low number of cells per unit length, this approximation for the local curvature is quite rough.

The most remarkable result seen in Fig. 2 is the large modulation of the tissue thickness in compact and invaginated folds. In the former, the largest thickness of the waveform is almost 200% of the smallest thickness (Fig. 2, *A* and *E*, *C1* and *C2*), and in the latter this ratio is ~150%. On the other hand, the thicknesses of evaginated and wavy folds are virtually uniform.

As per the reduced curvature, $c\lambda$ (Fig. 2, *B* and *F*), its alternating sign on going from the groove to the crest and to the next groove is of course expected, but the step-like profile seen in all fold morphologies is not. In turn, the sharp boundaries between the domains of positive and negative curvature imply that the ratio of the groove and crest curvatures, $-c_g/c_c$ (Fig. 1 *B*), can be used to identify a given fold type based on easily measurable quantities.

By comparing the thickness and curvature profiles for a given fold type in Fig. 2, *A* and *B*, we find that they are correlated in the sense that the maximal and the minimal thickness coincide with maximal and minimal curvature, respectively. On the other hand, those in Fig. 2, *E* and *F*, are anticorrelated. This effect is clearly seen in Fig. 2, *D* and *G*, where tissue thickness is plotted against curvature, the cell index running along each loop (the loops appear degenerated because the waveforms are almost perfectly symmetric). The thickness-curvature coupling is more prominent in compact and invaginated folds of either type but not in the evaginated and wavy folds, where tissue thickness does not vary much along the waveform. By comparing the parameters of these waveforms, we conclude that the nature of coupling is determined by the sign of the differential tension (correlation for $\alpha - \beta < 0$ and anticorrelation for $\alpha - \beta > 0$), whereas its magnitude increases with $|\alpha - \beta|$ and decreases with κ ; also important is cell-cell repulsion, which stabilizes the shape of most waveforms.

Although the four fold types are very distinct, the shape of the waveform changes continuously across the phase diagram (Fig. S8), and there exists no order parameter that could be used to precisely define the transitions between them. Thus, we resort to suitable auxiliary criteria to partition the phase space. For example, in the invaginated folds, the apical sides of some nonneighboring cells touch, but in the wavy folds, they do not due to the larger bending rigidity of the basement membrane, and so the invaginated-wavy transition can be associated with the point of detachment. Even though the thus-introduced boundaries between the fold morphologies in Fig. 1, *D* and *E*, are semiquantitative,

they suggest that compact, invaginated, and flat morphologies are rather robust in the sense that they occupy a considerable part of the phase diagram, whereas evaginated and wavy folds are more restricted. Qualitatively, we may conclude that 1) the compact folds are stable at large differential tensions, $|\alpha - \beta|$, and small basement-membrane bending moduli; 2) the invaginated folds are stabilized by a moderate bending modulus; and 3) the evaginated and wavy folds require that the basal tension be larger than the apical tension, but not very dramatically, and evaginated folds additionally rely on a flexible basement membrane.

In Fig. 1, *D* and *E*, we zoom into the part of the diagram where the differential tension, $|\alpha - \beta|$, is large enough to stabilize fold morphologies but still realistically moderate; the global topology of the phase diagram is discussed in Section S2. Finally, by changing tissue lateral tension defined by $\alpha + \beta$ (28) the results presented above can be readily adapted to describe columnar as well as cuboidal epithelia. Our results also provide an explanation of why squamous fold morphologies are rarely observed. Folds do require a certain minimal magnitude of the differential tension, $|\alpha - \beta| \geq 1.4$ (Section S1), and given that both α and β are positive, this implies that $\alpha + \beta$ must also be >1.4 . In this regime, cells are cuboidal or columnar rather than squamous.

DISCUSSION

Classification of observed fold morphologies

All four types of epithelial folds were identified in histological sections of invertebrate and vertebrate tissues reported in the literature or imaged in our laboratory. Compact $\beta > \alpha$ folds are present in the wing imaginal disc of *Drosophila* larva (Fig. 3 *A**) and in parts of cat lung bronchus (Fig. 3 *A***). Examples of invaginated $\alpha > \beta$ folds include intestinal epithelium of bony fishes (silver sailfin molly *Poecilia latipinna* (Fig. 3 *B**)) and the epithelium of mammalian colon (rat small intestine (Fig. 3 *B***)). The invaginated $\beta > \alpha$ folds are seen in cnidarian actinopharynx (*metridium* (Fig. 3 *C**)), and in vertebrate bronchiole (cow and mouse (Fig. 3, *C*** and *C****), where wavy folds are present, too (mouse (Fig. 3 *D****)). Wavy morphology is also found in the body surface of snail *Helix* sp. (Fig. 3 *D**) and in the hindgut of earthworm *Lumbricus* sp. (Fig. 3 *D***). The evaginated epithelium is identified in cat lung bronchiole (Fig. 3 *E**), in monkey oviduct (Fig. 3 *E***), and in trout intestine (Fig. 3 *E****). Additional physiological details are summarized in Section S3.

Each micrograph in Fig. 3 is combined with a theoretical waveform that fits the fold morphology in question, represented by individual cells if their boundaries are visible in the micrograph or by the contours if cell boundaries cannot be easily seen. The quantitative agreement of both large and fine features is quite good, despite the inherent fold-to-fold

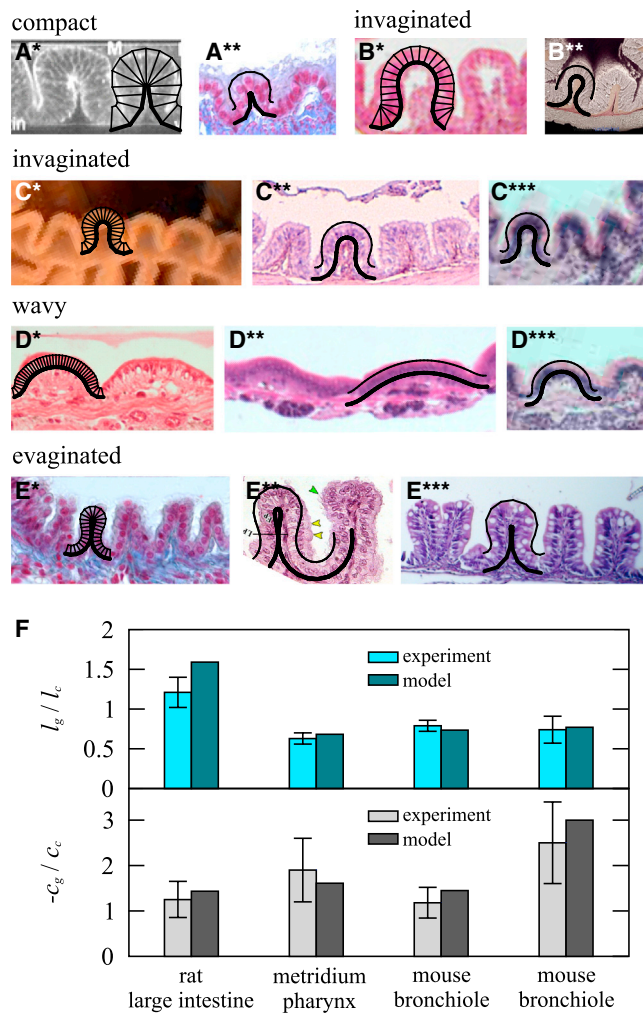


FIGURE 3 Examples of the four fold morphologies in vertebrates and invertebrates. Compact folds (A* and A**), invaginated folds with $\alpha > \beta$ (B* and B**) and $\beta > \alpha$ (C*–C***), wavy folds (D*–D***), and evaginated folds (E*–E***). (A*) is reproduced from Johnstone and Wells (45), published under Creative Commons license CC-BY; (B*) is reproduced with permission of the International Journal of Zoological Research from Mobarak and Sharaf (46); (B**) is reproduced with permission from Visuals Unlimited (<http://visuals unlimited.photoshelter.com/gallery-image/Dr-Richard-Kessel/G00002iBlh8co7x8/10000m18wfK0VDHU/C0000eOTVcBEMmtI>); (C*) is courtesy of M. Ford and J. Houseman (University of Ottawa; http://salinella.bio.uottawa.ca/BIO2135/labs/default.php?PoftheP/2012/Lab03/Lab03_Cnid.htm); (C**) is courtesy of P. W. L. Kwan (Tufts University School of Medicine; <http://ocw.tufts.edu/Content/4/coursehome/221120/221123>); (C***), (D*), (D**), and (D***) are courtesy of K. Perryman-Snow (<http://www.calpoly.edu/~eperryman/yewang/Home.htm>); (E*) and (E***) are courtesy of M. Moyal (Hebrew University of Jerusalem; <http://courses.md.huji.ac.il/histology/female/XIII-5.html>) and A. Ortiz (Norel Animal Nutrition), respectively. Micrographs (A**), (D*), (D**), and (E*) were taken in our laboratory. (F) Comparison of experimental and theoretical relative groove/crest tissue thickness and curvature in the folds from (B**), (C*), (C***), and (D***) (left to right). The parameter values of model folds that describe the experimental data (A*–E***) are listed in Table S1. To see this figure in color, go online.

variability natural in soft tissues and despite several methodological disadvantages. In particular, histological sections are usually not cut exactly perpendicular to the epithelial sheet nor to the folds, so the fold shape may appear distorted in various ways (Section S4); moreover, in real tissues cells are usually not strictly perpendicular to the contour of the epithelium, as theoretically predicted. Second, cell borders often cannot be precisely determined due to the limited resolution of the microscope and due to the presence of extracellular material near cell surfaces. Lastly, our model does not include several biological processes that too can affect epithelial shape, especially the presence of two or more cell populations in the tissue, cell division, and external forces due to muscle activity.

Epithelial morphometry

Despite these impediments, the quantitative comparison of theoretical and experimental fold shapes in Fig. 3, A*–E***, is convincing. Here, we present the relative groove/crest tissue thickness, l_g/l_c , and curvature, $-c_g/c_c$, as the most easily measurable features of the waveforms. In view of the well-defined step-like thickness and curvature profiles, their groove/crest variation can be considered representative of a given waveform, although in a dedicated experiment, one would ideally compare the whole contour. Fig. 3 F shows these two ratios in epithelia in the rat small intestine (Fig. 3 B**), in *metridium* actinopharynx (Fig. 3 C*), and in mouse bronchiole (Fig. 3 C*** and D***). In each image, tissue thickness and curvature were measured in the fold overlaid with the theoretical waveform, and error bars were determined by the inaccuracy of the cell border and the radii of curvature. The agreement found is good in all four cases, calling for further experimental studies permitting an in-depth morphometric analysis of samples with many waveforms.

Based on the measured values of l_g/l_c and $-c_g/c_c$, as well as on the overall shape of waveforms, we can roughly estimate the reduced differential tension and the reduced bending rigidity of the basement membrane of these epithelia (Section S5). In rat small intestine in Fig. 3 B**, $\alpha - \beta = 3.2$ and $\kappa = 0.4$; in *metridium* actinopharynx in Fig. 3 C*, $\alpha - \beta = -2.2$ and $\kappa = 0.14$, whereas in mouse bronchiole in Fig. 3 C***, $\alpha - \beta = -1.9$ and $\kappa = 0.1$ and in that in Fig. 3 D***, $\alpha - \beta = -2.2$ and $\kappa = 0.3$. Since we computed the minimal-energy shapes with a finite step in the model parameters (Section S2), the accuracy of these estimates is $\sim 20\%$, which is approximately the largest relative difference between two neighboring sets of parameters used in our computations.

The shape of the different epithelial folds formed during tissue development, differentiation, and performance depends on their function. Since any single epithelium usually simultaneously serves diverse purposes, it is difficult to establish a one-to-one correspondence between a

given function and a particular epithelial type. Nonetheless, in the examples collected in Fig. 3, such relations are indicated. Compact folds may be primarily associated with reducing the length of the sheet to minimize the area occupied by epithelial cells and allow occasional dilations or further growth (e.g., in embryos). Absorptive and secretory epithelial folds consist of invaginated or evaginated sheets with crests and grooves of various dimensions. In absorptive epithelia, crests are composed of either flattened or elongated cells with enlarged apical surface, which is consistent with the $\alpha > \beta$ variant of the invaginated fold morphology. Cells in the grooves are apically constricted, resulting in an increased cell height. On the other hand, in secretory epithelia, the crest cells are basally constricted and apically enlarged due to the intense secretion of fluids and mucus, and the grooves of epithelia are often widely open, i.e., their radius of curvature is large enough compared to wavelength so that non-neighboring cells in the region between the groove and the crest do not touch. Transportive epithelia may have wavy, invaginated, or evaginated fold morphologies with grooves of variable depths and widths, the folds enabling lumen distension for efficient transport of air and liquids in the grooves.

At this juncture, it is worthwhile comparing the fin-like shape of longitudinal folds with villi, finger-like protrusions into the lumen typical for mammalian small intestine. Villi that are closely spaced have a considerably larger excess surface area compared to folds, and thus a superior capacity for the absorption of nutrients. However, folded epithelia are more readily stretched or compressed in the direction perpendicular to the folds, thereby better accommodating changes in size of stroma and lumen distension due to external forces exerted, e.g., by surrounding muscles. In addition, these morphologies must have a very anisotropic bending rigidity much like common corrugated paper or even insect wings (39), their resistance to bending along folds being increased. Thus, the folded epithelia may well provide some structural support, which could be relevant in neutrally buoyant animals without a skeleton, like cnidaria. In addition, evaginated folds most probably bend less compared to villi of similar dimensions when fluids flow past them. This may well increase the volume and the residence time of the fluid trapped within the grooves, enhancing the retention capacity of the folds and contributing to more efficient adsorption. These ideas are related to elastic deformations of fold morphologies, which can be readily explored in a suitably extended version of our model.

A generalization is also needed to reproduce the evaginated longitudinal folds in the stomach of *Styela clava* (Fig. 12 of (40)), which are longer than in any waveform predicted here. The discrepancy is not surprising, because gastrointestinal epithelia are known to consist of two or more physically distinct cell populations, and by describing

each population by a different set of apical, lateral, and basal tensions it should be possible to improve agreement. This is most straightforwardly done by separating 1) a groove population with an increased apical tension from 2) a crest population with an increased basal tension by 3) an intervening population of cells without a differential apicobasal tension. Within such a model, fold shape could be tuned by adjusting the size of each cell population and its three effective tensions. It is conceivable that the postulated tension gradients along the waveform are associated with cell maturation and migration toward the crest, where they are shed (40). In a similar fashion, one could seek an explanation for the alternative major and minor folds seen in the stomach of *Ciona intestinalis* (Fig. 2 E of Ermak (41)).

Comparison to other theories

Each of our theoretical waveforms is characterized by a contour and a tissue thickness profile, and it is natural to ask whether the types of shapes reported here can be expected in other models. The existence of the folds themselves has been so far associated primarily with the area mismatch between the epithelium and the supporting stroma, typically due to certain dynamical processes within the epithelium, such as cell division and cell death (5–9). In the area-mismatch theory, the groove-crest asymmetry seen in shapes in Fig. 1 may be caused by the elasticity of the stroma at large deformations simply because the local displacement field immediately below the crest is not the mirror image of that below the grooves. This effect could well be enhanced by a suitable nonlinear elastic theory of the stroma, as well as by a curvature-dependent cell division rate (5) or an inhomogeneous preferred curvature of the basement membrane, which can be adjusted to control the shape of the waveform (34). Whether the ensuing asymmetry of the folds is as pronounced as in our waveforms, and whether the fold types generated by area mismatch agree with those proposed here, remains an open question to be resolved numerically. Alternatively, tissue buckling may be triggered by differential mechanical properties of cells, which could be efficiently implemented within a nonplanar vertex model representing the apical sides (42,43), where deformation can be caused by a suitable pattern of, e.g., cell-cell tension. One of the advantages of this approach is that it allows one to more straightforwardly include cell rearrangements, which is probably important in the formation of crypts and villi for topological reasons.

In turn, the nonplanar vertex model does not address the tissue thickness, and in the area-mismatch theory, thickness is fixed. Although the specific buckling scenarios discussed above can in principle produce contours similar to our waveforms, it is more difficult to see how they could give rise to the distinct tissue thickness profiles, some of which are quite

pronounced, as shown in Fig. 2, A and E. This previously overlooked morphometric feature can be used to estimate the intracellular tensions, as well as to compare the different models to experimental data. Fig. 4 illustrates the difference between folds generated by area mismatch and by intraepithelial stress. Fig. 4 A shows an epithelium at $\alpha - \beta = 0$ that is buckled because of confinement mimicking competition between tissue growth and restoring elastic forces (5). Here, thickness does not vary along the tissue. The waveform in Fig. 4 B corresponds to the same epithelium additionally supported by a very rigid basement membrane with $\kappa = 2$, which does lead to slightly nonuniform thickness varying over a range of 1% of the average. The bottom waveform (Fig. 4 C) is our invaginated morphology with a finite apicobasal differential tension leading to a very pronounced thickness modulation with a range of about 30%. Based on such differences, one can distinguish between the possible mechanisms at work, provided, of course, that cells in the tissue can be assumed to be mechanically identical.

CONCLUSIONS

The agreement of theoretical and experimental fold morphologies reported here supports the intraepithelial stress hypothesis, suggesting that cell-level forces and cell-cell adhesion may well be directly responsible for the observed morphologies. This view complements the area-mismatch theories where the corrugated shape of epithelia is attributed to tissue growth and cell division. The theoretical waveforms obtained allowed us to distinguish between four types of folds, and we wish that the proposed classification were

further elaborated. Our model also predicts fold morphologies in columnar and cuboidal, but not in squamous, epithelia which is consistent with most experimental data and implies that the rare cases of folded squamous epithelial tissues should be generated by an alternative mechanism and not by apicobasal tension.

There are several ways of improving our theory. First, a three-dimensional implementation of the model should be able to reproduce zig-zag folds with a characteristic fish-bone in-plane pattern (8), as well as villi and crypt morphologies, where the intraepithelial stresses are expected to play an even more important role for purely geometrical reasons (28). Second, the model can be readily extended to pseudostriated epithelia, say, by including a finite-sized nucleus, which could be located either at the apical or at the basal side in very tall cells. The disposition of nuclei can be both the origin and the result of tissue deformation, and we expect that the phase diagram of this extended model should contain more fold waveforms than the current version. Third, our ideas may be generalized by including cell division and cell death as two mechanisms controlling buckling within the area-mismatch theory, which could well give rise to an even more diverse spectrum of waveforms (5). We are hopeful that the theoretical predictions available will stimulate further detailed morphometric studies of the various epithelial morphologies, leading to a quantitative understanding of the mechanics involved.

SUPPORTING MATERIAL

Supporting Materials and Methods, eleven figures, and one table are available at [http://www.biophysj.org/biophysj/supplemental/S0006-3495\(15\)01205-9](http://www.biophysj.org/biophysj/supplemental/S0006-3495(15)01205-9).

AUTHOR CONTRIBUTIONS

P.Z. designed research; N.Š., M.K., P.M., and J.Š. performed research; N.Š., M.K., P.M., J.Š., and P.Z. wrote the manuscript.

ACKNOWLEDGMENTS

We thank P.-F. Lenne, G. Tkačik, and R. Winklbauer for stimulating discussions and J. Houseman, P. W. L. Kwan, M. Moyal, A. Ortiz, and K. Perryman-Snow for providing us with the micrographs used in Fig. 3.

This work was supported by the Slovenian Research Agency through grants P1-0184 and P1-0055, the Marie-Sklodowska-Curie European Training Network COLLDENSE (H2020-MSCA-ITN-2014 Grant No. 642774), and the European Science Foundation Research Networking Programme QuanTissue.

REFERENCES

1. Bowden, N., S. Brittain, ..., G. M. Whitesides. 1998. Spontaneous formation of ordered structures in thin films of metals supported on an elastomeric polymer. *Nature*. 393:146–149.

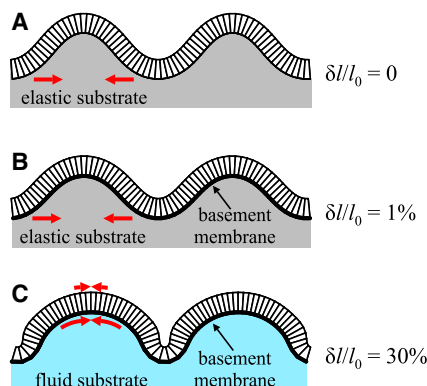


FIGURE 4 Comparison of fold morphologies in growing tissue characterized by area mismatch (A) (no basement membrane, $\alpha = \beta = 1.9$) and (B) (basement membrane of $\kappa = 2$ included) and in an invaginated epithelium with a finite apicobasal differential tension (C) ($\alpha = 0.6$, $\beta = 3.2$, and $\kappa = 0.6$); the parameters were chosen so that the wavelength and number of cells per fold are similar to those in (A) and (B). The relative percentages of thickness modulation are 0, 1%, and 30%, respectively. Arrows indicate that folds in (A) and (B) are stabilized by area mismatch and the elasticity of stroma, whereas that in (C) is due to apicobasal differential tension. To see this figure in color, go online.

2. Genzer, J., and J. Groenewold. 2006. Soft matter with hard skin: From skin wrinkles to templating and material characterization. *Soft Matter*. 2:310–323.
3. Brau, F., H. Vandeppar, ..., P. Damman. 2010. Multiple-length-scale elastic instability mimics parametric resonance of nonlinear oscillators. *Nat. Phys.* 7:56–60.
4. Wang, Q., and X. Zhao. 2015. A three-dimensional phase diagram of growth-induced surface instabilities. *Sci. Rep.* 5:8887.
5. Hannezo, E., J. Prost, and J. F. Joanny. 2011. Instabilities of monolayered epithelia: shape and structure of villi and crypts. *Phys. Rev. Lett.* 107:078104.
6. Ciarletta, P., and M. Ben Amar. 2012. Pattern formation in fiber-reinforced tubular tissues: folding and segmentation during epithelial growth. *J. Mech. Phys. Solids*. 60:525–537.
7. Ben Amar, M., and F. Jia. 2013. Anisotropic growth shapes intestinal tissues during embryogenesis. *Proc. Natl. Acad. Sci. USA*. 110:10525–10530.
8. Shyer, A. E., T. Tallinen, ..., L. Mahadevan. 2013. Villification: how the gut gets its villi. *Science*. 342:212–218.
9. Ciarletta, P., V. Balbi, and E. Kuhl. 2014. Pattern selection in growing tubular tissues. *Phys. Rev. Lett.* 113:248101.
10. Ferri, S., L. C. U. Junqueira, ..., L. O. Medeiros. 1976. Gross, microscopic and ultrastructural study of the intestinal tube of *Xenodon merremii* Wagler, 1824 (Ophidia). *J. Anat.* 121:291–301.
11. McAvoy, J. W., and K. E. Dixon. 1978. Cell specialization in the small intestinal epithelium of adult *Xenopus laevis*: structural aspects. *J. Anat.* 125:155–169.
12. Drasdo, D. 2000. Buckling instabilities of one-layered growing tissues. *Phys. Rev. Lett.* 84:4244–4247.
13. Kim, P., M. Abkarian, and H. A. Stone. 2011. Hierarchical folding of elastic membranes under biaxial compressive stress. *Nat. Mater.* 10:952–957.
14. Hohlfeld, E., and L. Mahadevan. 2011. Unfolding the sulcus. *Phys. Rev. Lett.* 106:105702.
15. Li, B., Y. P. Cao, ..., H. Gao. 2012. Mechanics of morphological instabilities and surface wrinkling in soft materials: a review. *Soft Matter*. 8:5728–5745.
16. Lecuit, T., and P. F. Lenne. 2007. Cell surface mechanics and the control of cell shape, tissue patterns and morphogenesis. *Nat. Rev. Mol. Cell Biol.* 8:633–644.
17. He, L., X. Wang, ..., D. J. Montell. 2010. Tissue elongation requires oscillating contractions of a basal actomyosin network. *Nat. Cell Biol.* 12:1133–1142.
18. Luu, O., R. David, ..., R. Winklbauer. 2011. Large-scale mechanical properties of *Xenopus* embryonic epithelium. *Proc. Natl. Acad. Sci. USA*. 108:4000–4005.
19. Tepass, U., and E. Knust. 1993. *crumbs* and *stardust* act in a genetic pathway that controls the organization of epithelia in *Drosophila melanogaster*. *Dev. Biol.* 159:311–326.
20. Dawes-Hoang, R. E., K. M. Parmar, ..., E. F. Wieschaus. 2005. Folded gastrulation, cell shape change and the control of myosin localization. *Development*. 132:4165–4178.
21. Mammoto, T., and D. E. Ingber. 2010. Mechanical control of tissue and organ development. *Development*. 137:1407–1420.
22. Martin, A. C., M. Gelbart, ..., E. F. Wieschaus. 2010. Integration of contractile forces during tissue invagination. *J. Cell Biol.* 188:735–749.
23. Lewis, W. H. 1947. Mechanics of invagination. *Anat. Rec.* 97:139–156.
24. Leptin, M. 2005. Gastrulation movements: the logic and the nuts and bolts. *Dev. Cell*. 8:305–320.
25. Rauzi, M., A. Hočevár Brezavšček, ..., M. Leptin. 2013. Physical models of mesoderm invagination in *Drosophila* embryo. *Biophys. J.* 105:3–10.
26. Derganc, J., S. Svetina, and B. Žekš. 2009. Equilibrium mechanics of monolayered epithelium. *J. Theor. Biol.* 260:333–339.
27. Hočevár Brezavšček, A., M. Rauzi, ..., P. Zihlerl. 2012. A model of epithelial invagination driven by collective mechanics of identical cells. *Biophys. J.* 103:1069–1077.
28. Krajnc, M., N. Štorgel, ..., P. Zihlerl. 2013. A tension-based model of flat and corrugated simple epithelia. *Soft Matter*. 9:8368–8377.
29. Hannezo, E., J. Prost, and J. F. Joanny. 2014. Theory of epithelial sheet morphology in three dimensions. *Proc. Natl. Acad. Sci. USA*. 111:27–32.
30. Steinberg, M. S. 1963. Reconstruction of tissues by dissociated cells. Some morphogenetic tissue movements and the sorting out of embryonic cells may have a common explanation. *Science*. 141:401–408.
31. Candiello, J., M. Balasubramani, ..., H. Lin. 2007. Biomechanical properties of native basement membranes. *FEBS J.* 274:2897–2908.
32. Ilina, O., and P. Friedl. 2009. Mechanisms of collective cell migration at a glance. *J. Cell Sci.* 122:3203–3208.
33. Landau, L. D., and E. M. Lifshitz. 1986. Theory of Elasticity. Pergamon Press, Oxford, United Kingdom.
34. Dunn, S.-J., A. G. Fletcher, ..., J. M. Osborne. 2012. Modelling the role of the basement membrane beneath a growing epithelial monolayer. *J. Theor. Biol.* 298:82–91.
35. D'Antonio, G., P. Macklin, and L. Preziosi. 2013. An agent-based model for elasto-plastic mechanical interactions between cells, basement membrane and extracellular matrix. *Math. Biosci. Eng.* 10:75–101.
36. Farhadifar, R., J. C. Röper, ..., F. Jülicher. 2007. The influence of cell mechanics, cell-cell interactions, and proliferation on epithelial packing. *Curr. Biol.* 17:2095–2104.
37. Odell, G. M., G. Oster, ..., B. Burnside. 1981. The mechanical basis of morphogenesis. I. Epithelial folding and invagination. *Dev. Biol.* 85:446–462.
38. Brakke, K. 1992. The Surface Evolver. *Exp. Math.* 1:145–165.
39. Rees, C. J. C. 1975. Form and function in corrugated insect wings. *Nature*. 256:200–203.
40. Ermak, T. H. 1975. Cell proliferation in the digestive tract of *Styela clava* (Urochordata: Ascidiacea) as revealed by autoradiography with tritiated thymidine. *J. Exp. Zool.* 194:449–466.
41. Ermak, T. H. 1981. A comparison of cell proliferation patterns in the digestive tract of ascidians. *J. Exp. Zool.* 217:325–339.
42. Osterfield, M., X. Du, ..., S. Y. Shvartsman. 2013. Three-dimensional epithelial morphogenesis in the developing *Drosophila* egg. *Dev. Cell*. 24:400–410.
43. Murisic, N., V. Hakim, ..., B. Audoly. 2015. From discrete to continuum models of three-dimensional deformations in epithelial sheets. *Biophys. J.* 109:154–163.
44. Ermak, T. H. 1982. The renewing cell populations of ascidians. *Am. Zool.* 22:795–805.
45. Johnstone, K., R. E. Wells, ..., M. P. Zeidler. 2013. Localised JAK/STAT pathway activation is required for *Drosophila* wing hinge development. *PLoS One*. 8:e65076.
46. Mobarak, Y. M. S., and M. M. Sharaf. 2011. Lead acetate-induced histopathological changes in the gills and digestive system of silver sailfin molly (*Poecilia latipinna*). *Int. J. Zool. Res.* 7:1–18.